Feasibility study on photovoltaic module-integrated planar air-core inductors to facilitate embedded power electronics

van Nijen, David A.; Chakravarty, Saurabh; Voorn, Jim; Zeman, Miro; Isabella, Olindo; Manganiello, Patrizio

DOI
10.1016/j.egyr.2024.12.003

Publication date
2025

Document Version
Final published version

Published in
Energy Reports

Energy Reports 13 (2025) 82–89

Contents lists available at ScienceDirect

Energy Reports

journal homepage: www.elsevier.com/locate/egyr

Research paper

Feasibility study on photovoltaic module-integrated planar air-core inductors to facilitate embedded power electronics

David A. van Nijen *, Saurabh Chakravarty, Jim Voorn, Miro Zeman, Olindo Isabella *, Patrizio Manganiello

Delft University of Technology, Mekelweg 4, Delft, 2628 CD, The Netherlands

ARTICLE INFO

Dataset link: http://doi.org/10.4121/b7267f87-15b1-4c97-b9b2-e3aeb95393ac

Keywords:
Photovoltaics
Photovoltatronics
Inductor
Power converter

ABSTRACT

Photovoltaic modules are typically not optimized for conditions of partial shading. One proposed approach to improve their shade tolerance is to implement maximum power point tracking on different strings of cells within the modules. However, this approach increases the demand for sub-module power converters, which poses a challenge. To address this, researchers have suggested integrating power electronic components directly into the module laminate, or even within the solar cells themselves. Despite these advancements, limited research has focused on integrating the most bulky component: the inductor. This study investigates through simulations whether planar air-core inductors can yield the required properties to support sub-module power conversion. The simulated inductors have an area that is as large as an industrial crystalline silicon solar cell. First, it is shown how the interplay between the different design parameters, such as track spacing, track width, number of turns, and middle gap size, plays an important role in the inductor properties at high frequency. The coil geometries that are simulated yield inductance values between 0.3 μH and 3.2 μH. Subsequently, the feasibility of implementing these inductors into an exemplary DC–DC boost converter is evaluated. To adequately reduce the ripple current, a significant switching frequency of at least several hundred kHz is required. Additionally, at 500 kHz, an inductor thickness of around 0.5 mm is necessary to keep the ohmic losses in the inductor below 2% of the total generated power in standard test conditions. While demonstrating feasible combinations, these findings also present significant challenges.

1. Introduction

The photovoltaic (PV) industry mainly produces crystalline silicon (c-Si) based modules with standardized designs, aimed at producing cheap power under uniform irradiation (Ziar et al., 2021). However, such modules do not perform optimally in locations where partial shading is common, such as in urban environments. Here, the adoption of so-called shade-tolerant PV modules has the potential to boost energy yield by up to 11%–30% (Olalla et al., 2014; MacAlpine et al., 2013; Calcabrini et al., 2021). To increase the shade tolerance of PV modules, one effective method is the implementation of maximum power point tracking (MPPT) at the sub-module level (Deline et al., 2014; Golroodbari et al., 2018; Stauth et al., 2012; Olalla et al., 2013; Leuenberger and Biela, 2017). This approach allows the operating point of groups of solar cells to be adapted without affecting the operation of the other cells in the PV module. Implementing sub-module MPPT can not only increase energy yield but may also extend the lifetime of the PV system by up to 10 years (Olalla et al., 2017). Although sub-module power electronics (PE) can be integrated into the junction box (Pilawa-Podgurski and Perreault, 2013), the increased demand for sub-module power converters poses a challenge. To address this challenge and facilitate the design of PV modules with a higher granularity of sub-module power converters, integrating (part of) the power electronic components into or onto the c-Si solar cells could be advantageous (van Nijen et al., 2022). Despite its challenges, such as thermal management and repairability, this approach also paves the way for the development of smaller sub-module converters with fewer power electronic components. One example of this integration involves incorporating transistors into the c-Si solar cells (van Nijen et al., 2024; Imtiaz et al., 2013; Imtiaz and Khan, 2013, 2012). Another example is to embed electrolytic plate-plate capacitors into photovoltaic cell laminates (Van Dyck et al., 2024). Additionally, c-Si solar cells exhibit notable intrinsic capacitive effects, which can be exploited in different applications (van Nijen et al., 2023, 2025; Chang et al., 2015; Huang et al., 2016). Furthermore, while inductors often emerge as the largest and most expensive components in power converters (Lai and Nelson, 2007; Burger and Kranzer, 2009; Ki and

* Corresponding authors.
E-mail addresses: d.a.vannijen@tudelft.nl (D.A. van Nijen), o.isabella@tudelft.nl (O. Isabella).

https://doi.org/10.1016/j.egyr.2024.12.003
Received 8 August 2024; Received in revised form 28 November 2024; Accepted 1 December 2024
Available online 9 December 2024

Ma, 2001; Sullivan and Sanders, 1996), the possibility of removing them from sub-module power converters and integrating them directly into the PV laminate remains relatively unexplored. Nevertheless, it is important to acknowledge several relevant publications. For instance, the design of small-area planar inductors has been explored (Dhahri et al., 2016), with implementation into a 6 MHz DC–DC converter for PV applications reported in a later publication (Dhahri et al., 2017). Their approach is similar to the fabrication of thin-film inductors in integrated circuits, typically created by forming spiral-like metallization patterns on silicon wafers (Sze, 2002). Additionally, amorphous silicon solar cells have been integrated onto flexible sheets along with wireless power delivery circuits that include thin-film inductors (Rieutort-Louis et al., 2014). However, these publications typically report lower current levels than those produced by industrial photovoltaic cells. For applications involving higher power levels, publications involving planar inductors can be found within the field of wireless power transfer. There, planar inductor structures with outer diameters ranging from 10 cm to 20 cm have been reported, exhibiting inductance values between 3.13 μH and 80 μH (Li and Costinett, 2018; Acero et al., 2013; Varghese et al., 2017; Low et al., 2009, 2010; Casanova et al., 2009). However, due to their relatively high parasitic resistances, typically in the hundreds of milliohms, these coils are generally not suitable for direct use in photovoltaic sub-module converters. More relevant to the topic of this paper, previous work explored the integration of large-area inductors onto c-Si solar cells, as well as the route of enhancing solar cell self-inductance by redesigning the metallization pattern (van Nijen et al., 2022). While the study concluded that solar cells provide sufficient area for integrating planar inductors, detailed descriptions of the optimal inductor design for such applications are still lacking. Furthermore, studies have demonstrated that employing planar inductors in PV module-integrated inverters can facilitate the development of wireless PV modules (Carigiet, 2022; Carigiet et al., 2018, 2019). Finally, it is worth mentioning a study where a dual-layer inductor with a volume of 12 mm $\times$ 12 mm $\times$ 10 mm is optimized for implementation into a DC–DC boost converter for PV applications (Benzidane et al., 2022).

Before discussing the integration of inductors into PV modules, it is important to consider how the required inductor properties are influenced by the power converter. In DC–DC converters, minimizing ripple current in the inductor is preferable, but the required inductance to achieve this is frequency-dependent (Ayop and Tan, 2018). Specifically, increasing the switching frequency reduces the required inductance, which in turn decreases the cost and size of the inductor (Wang et al., 2020). Here, it is worth noting that every conductor exhibits at least some inductance. Thus, pushing this concept to its limit involves exploiting the natural inductance exhibited by solar cells at the input of a converter to the point where a physical inductor becomes unnecessary (Huang et al., 2016). Switch-mode converters that normally have their inductor at the input of the converter could be suitable candidates for this concept. However, to achieve a sufficiently low current ripple with this approach, a switching frequency of at least several MHz may be required, as demonstrated in the calculation for an exemplary boost converter shown in Appendix A. For a switch-mode converter, this switching frequency can lead to high losses. In general, it must be acknowledged that increasing the switching frequency also comes with the disadvantages of (1) higher switching power losses, (2) increased inductor core losses, and (3) heightened electromagnetic interference.

An intermediate approach in between conventional sub-module converters and high-frequency converters that leverage the solar-cell self-inductance could be to integrate inductors at a sub-module level. By selecting a planar inductor structure, they could potentially be embedded within the PV laminate. For instance, this integration could be done by directly integrating the inductor on the back of a PV cell (van Nijen et al., 2022). Alternatively, other module-integration methods, such as combinations with three-dimensional-woven interconnection fabrics (Van Dyck et al., 2021) or conductive interconnection foils (Lamers et al., 2012), could be worth exploring. Successfully integrating inductors in such a way can enhance the inductance of a solar-cell string when connected in series. Subsequently, this can be leveraged in combination with converter topologies that incorporate an inductor at the input. Additionally, the planar inductors offer flexibility in their connection configurations, allowing the inductance to be used in converter topologies with inductors located in other parts of the circuit. However, to assess the integration feasibility, it is crucial to understand the design requirements of the inductor itself. A common approach to enhance the inductance of an inductor involves using a ferromagnetic core made of material with large magnetic permeability. This study, however, investigates planar inductors without such a core. Since the common PV-module materials such as silicon, encapsulants, glass, copper, aluminum etc., all have a relative magnetic permeability close to one – similar to the magnetic permeability of vacuum and air – this design is referred to as *air-core* inductors. Specifically, we explore how the planar air-core inductor design can be adjusted to achieve the desired inductor performance and evaluate the feasibility of integrating these inductors into a sub-module-level power converter. All inductors in this study use copper as their conductor material, which their area fixed at 12.5 cm $\times$ 12.5 cm, which is the maximum available area for a 5-inch solar cell (Sunpower, 2022). On the one hand, air-core inductors offer simple manufacturing and eliminate core losses during operation. On the other hand, achieving sufficiently high inductance can be challenging. This necessitates operation at relatively high switching frequency, which can adversely affect inductor performance. While high-frequency effects could be partly mitigated by using Litz wires (Wojda and Kazimierczuk, 2018), this contradicts the goal of simplified manufacturing. Therefore, this study evaluates the potential of the more simple planar inductor designs, despite the high-frequency effects.

This study employs a finite element model, which is introduced in Section 2. This is followed by an analysis of how various inductor design parameters affect the performance in Section 3. The feasibility for integration into sub-module power converters is discussed in Section 4, followed by the conclusions in Section 5.

2. Simulation method

Fig. 1(a) shows an example of how the inductor can be integrated at a sub-module level (van Nijen et al., 2022). In this configuration, the inner terminal of the planar inductor is connected to the metal back-side of a PV cell, while the outer terminal can be connected to an external circuit. Apart from this internal connection, the inductor is separated from the PV cell by an electrically insulating layer, which could be either encapsulant material or a dielectric layer. The inductance of a planar inductor is the sum of the self-inductances of the individual metal segments and the mutual inductances between them (Greenhouse, 1974; Shaltout and Gregori, 2020). Although analytical expressions for calculating the inductance of planar inductors have been reported (Mohan et al., 1999), it is important to note that these expressions are only valid for specific ranges of coil geometries and frequency ranges. For instance, in practical applications such as power converters, the inductor is subjected to a ripple current at a certain frequency. At sufficiently high frequencies, this introduces phenomena such as the skin effect and proximity effect. Skin effect is the phenomenon where alternating current tends to concentrate near the surface of the conductor at high frequencies (Nguyen and Fortin Blanchette, 2020). This occurs due to the eddy currents that are induced by the time-varying magnetic field. Additionally, the proximity effect is caused by magnetic interaction between different segments of the inductor track. The time-varying magnetic fields generated by neighboring segments further modify the current distribution, leading to a higher current density at the edges of the track (Cao et al., 2003).

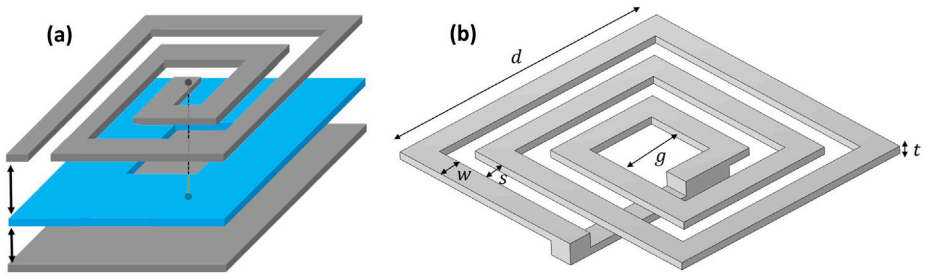

Fig. 1. (a) Example configuration of how a planar inductor could be integrated at a sub-module level. Whereas the inner terminal of the inductor is connected to the back-side of a PV cell, the rest is separated by an electrically insulating layer. Moreover, (b) shows the geometry of an example three-turn inductor structure as modeled in this study. Various design parameters are indicated; the outer diameter (d), internal diameter or middle gap (g), track spacing (s), track width (w), and thickness (t).

Due to these high-frequency effects, the resistance and inductance values may differ under direct current (DC) and alternating current (AC) conditions, both of which are often relevant for implementation in a power converter. To analyze the inductance and resistance for planar inductor structures such as the one in Fig. 1(a) while accounting for high-frequency effects, the planar inductors in this study are analyzed using the finite element method simulator COMSOL (COMSOL Group, 2022). Specifically, a three-dimensional inductor geometry, as depicted in Fig. 1b, is investigated. The analysis is performed using the magnetic fields interface, which solves Maxwell's equations. This solution is computed in the frequency domain, meaning it is based on a sinusoidal current excitation at a fixed frequency. By calculating the magnetic field and induced current distributions within the inductor, the simulation provides both an inductance value and a resistance value for each tested geometry. The details and equations supporting these computations are outlined in the AC/DC module user's guide of COMSOL (COMSOL, 2022). In the simulated geometries, the inner and outer terminals of the inductor are connected to form a closed-loop design to comply with the current conservation inherent in Ampère's law. While not shown in Fig. 1b, the inductor geometry is positioned within a spherical air domain, with an infinite element domain at the outer boundary to emulate a domain of infinite extent. This configuration ensures accurate simulation of the magnetic field lines, resulting in precise inductance values. The inductor itself is made of copper with a conductivity of 5.998×10^7 S/m and the temperature is set at 20 °C. It is important to mention that since the coil is surrounded by air, parasitic phenomena that may occur between the coil and substrate in the eventual application are not considered in this analysis. Various coil design parameters, as indicated in Fig. 1b, are examined in this study. These parameters include the internal diameter or middle gap (g), track spacing (s), track width (w), and thickness (t). The outer diameter (d) is fixed at 12.5 cm to optimize the inductor design while ensuring it fits within the area of an industrial solar cell.

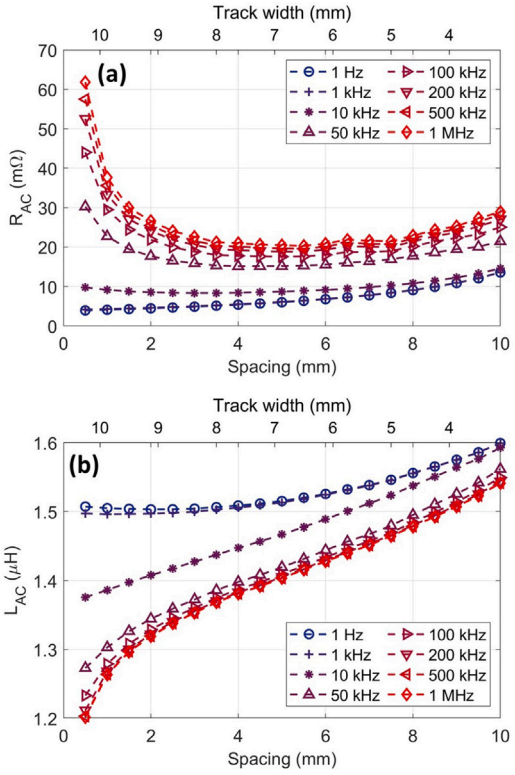

Fig. 2. The (a) R_{AC} and (b) L_{AC} of a planar inductor are plotted as a function of spacing (primary horizontal axis) and width (secondary horizontal axis). The inductor structure consists of 4 turns, with an outer diameter d of 12.5 cm, a middle gap g of 4 cm, and a thickness t of 0.5 mm.

3. Inductor design results

This section describes how the inductor properties change with design and frequency variations, focusing primarily on AC inductance (L_{AC}) and AC resistance (R_{AC}). At relatively low frequencies below 1 kHz, the high-frequency effects in the studied inductor geometries diminish, causing the 1 Hz values to converge to the DC inductance (L_{DC}) and DC resistance (R_{DC}).

3.1. Spacing/width variation

The effect of track spacing (s) on inductor performance, with d and g held constant, is illustrated in Fig. 2. Notably, an increase in track spacing corresponds to a decrease in w. The results are for a 4-turn coil with a gap of 4 cm and a thickness of 0.5 mm.

Fig. 2(a) demonstrates that at low frequencies, minimizing s while maximizing w leads to the lowest R_{AC} values. This is as expected, since a high w maximizes the cross-section of the track. However, maximizing w and minimizing s does not necessarily yield the lowest R_{AC} values at high frequencies. For air-core inductors, it is known that the resistance may increase at high frequency due to the skin effect and the proximity effect (Kolahian et al., 2024). Which of these two mechanisms dominates the increase in resistance depends on the inductor geometry. For instance, at frequencies of 50 kHz and higher, Fig. 2(a) shows that there is significant increase in R_{AC} when s decreases below 2 mm. This shows that a minimum spacing is required to limit the proximity effect. Conversely, increasing s beyond approximately 6 mm also leads to a higher R_{AC}, attributed to the increase in DC wire resistance due to reduced w. Thus, for frequencies above 50 kHz, R_{AC} reaches its minimum around a spacing of 4–6 mm. However, even at this spacing, there is still a notable increase in R_{AC} with increasing frequency, which can presumably be mostly attributed to the skin effect in the inductor's track. The occurrence of the skin effect at high frequencies is an inherent limitation of the chosen design. While out

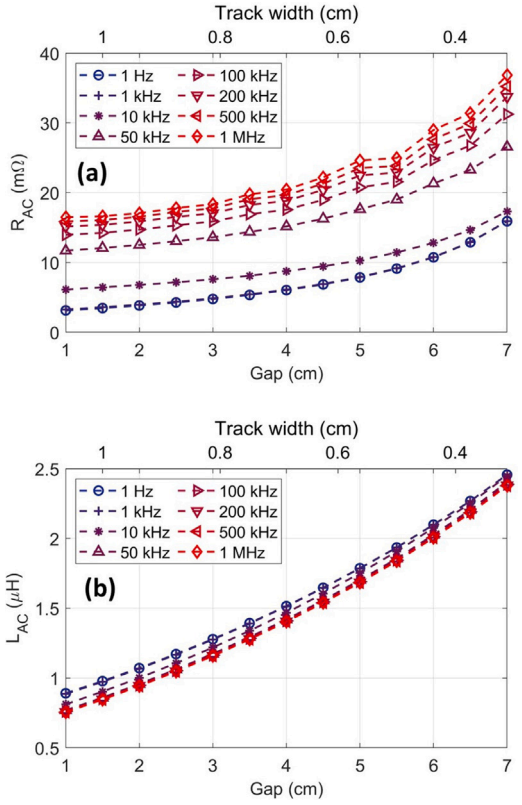

Fig. 3. The (a) R_{AC} and (b) L_{AC} of a planar inductor are plotted as a function of gap size (primary horizontal axis) and width (secondary horizontal axis). The inductor structure consists of 4 turns, with an outer diameter d of 12.5 cm, a spacing s of 5 mm, and a thickness t of 0.5 mm.

of the scope of this study, a discussion on the use of alternative track structures such as multitrack, in-layer twisted, or Litz structures is reported in Kolahian et al. (2024).

In Fig. 2(b), it is evident that for both low and high frequency, an increase in s is accompanied by an increase in L_{AC}. At low frequencies, this is mostly related to the fact that an increase in s corresponds to a decrease in w. Previous work has shown that structures with smaller cross-sections tend to exhibit higher inductance values (Kolahian et al., 2024). The reason behind this phenomenon is that the magnetic field becomes more concentrated around the conductor, resulting in higher self-inductance (Rosa, 1908). Indeed, through additional COMSOL simulations for a straight wire we have confirmed that the relative increase in L_{AC} as w decreases is similar (not shown). Furthermore, Fig. 2(b) shows that higher frequencies reduce L_{AC} for all tested geometries. This is related to the well-established phenomenon that the self-inductance of wires decreases as the current distribution over their cross-section changes with increasing frequencies (Coffin, 1906). It is important to note that the decrease in L_{AC} with frequency is more pronounced for low s values than for high s values. At higher s values, the change is primarily due to the skin effect, while at lower s values, both the skin effect and proximity effect contribute to the alteration in current distribution.

The interplay between s and w significantly influences the quality factor of the inductor. The quality factor Q is defined as $Q = 2\pi f L_{AC}/R_{AC}$, with f representing the frequency. For frequencies between 10 kHz and 1 MHz, the highest Q value is observed within the spacing range of 4 mm to 6 mm. However, it must be noted that the highest Q does not necessarily correspond to the optimal coil for integration into a power converter, as R_{DC} can also play an important role.

3.2. Gap/width variation

The effect of the middle gap (g) on the inductor performance is shown in Fig. 3. The results are for a 4-turn coil with a spacing of 5 mm and a thickness of 0.5 mm. Since d and s are held constant, an increase in g results in a decrease in w. Additionally, a larger g results in an increase in the total track length.

Fig. 3(a) illustrates that a higher g correlates with an increase in R_{AC} across all tested frequencies. At low frequencies, this effect is due to both the smaller cross-section of the track and the increased total track length. However, at higher frequencies, the relative increase in R_{AC} due to an increase in g becomes smaller. For instance, at 1 Hz the R_{AC} increases a factor ∼5.1 when g is increased from 1 cm to 7 cm, whereas this is only a factor ∼2.2 for 1 MHz. This difference is mainly attributed to the skin effect, which causes the current to concentrate at the edges of the wire at high frequencies. Consequently, a reduction in w has a diminished impact on the R_{AC} at high frequency.

In Fig. 3(b), it is evident that increasing g significantly increases the L_{AC} across all tested frequencies, which aligns with expectations (Kolahian et al., 2024). This behavior can be understood by considering that inductors with larger g have their inner turns positioned further from the center of the spiral. Consequently, these turns contribute more positive mutual inductance and less negative mutual inductance (Mohan et al., 1999). More theoretical background on the positive and negative mutual inductances within different segments of a planar inductor has been reported by Greenhouse (Greenhouse, 1974). Additionally, the increase in L_{AC} with higher g is partly attributed to the longer track length and the reduced w.

For low frequencies of 1 Hz and 1 kHz, the quality factor Q reaches its peak when the gap is minimized to 1 cm. However, as the frequency increases to 50 kHz and beyond, the optimal range for Q shifts to a range where the g value lies between 4 cm and 7 cm. A slightly declining trend in Q is observed beyond 5.5 cm.

3.3. Number of turns vs gap/width variation

In the preceding section, it was demonstrated that increasing the middle gap (g) significantly contributes to enhancing inductance. However, another viable method for boosting inductance is by increasing the number of turns (N). Indeed, it is expected from literature that the inductance increases quadratically with the number of turns when d and g are held constant (Mohan et al., 1999). This raises the question of whether a high g or a high N yields the best inductor performance, characterized by a high inductance and low resistance. Fig. 4 presents L_{AC} at 500 kHz plotted as a function of (a) R_{DC} and (b) of R_{AC}. The data in Fig. 4 are obtained for coils with varying number of turns and gap sizes. Optimal performance would position the data in the top left quadrant of these figures. However, it is evident from both Fig. 4(a) and Fig. 4(b) that a trade-off exists in the design. While L_{AC} can be increased by raising either N or g, this inevitably leads to higher R_{DC} and R_{AC} values. The changes in R_{DC} and R_{AC} result from the combined effects of variations in the total track length and the track's width. Such trade-offs between inductance and resistance are commonly encountered in inductor design (Shaltout and Gregori, 2020). It is worth noting that the inductor thickness (t) is a parameter that can still be varied, exerting limited influence on the inductance but affecting the resistance. This means that by varying t, the data in Fig. 4 can be shifted horizontally, to a certain extent allowing for the adjustment of the resistance to the desired value. However, in this work a maximum t of 1 mm is used, since coils with higher t consume more material, are more difficult to manufacture, and can pose practical challenges for integration into a PV module.

4. PV module integration feasibility

Now that the inductor design considerations have been investigated, the next step is to assess whether these coils possess the desired

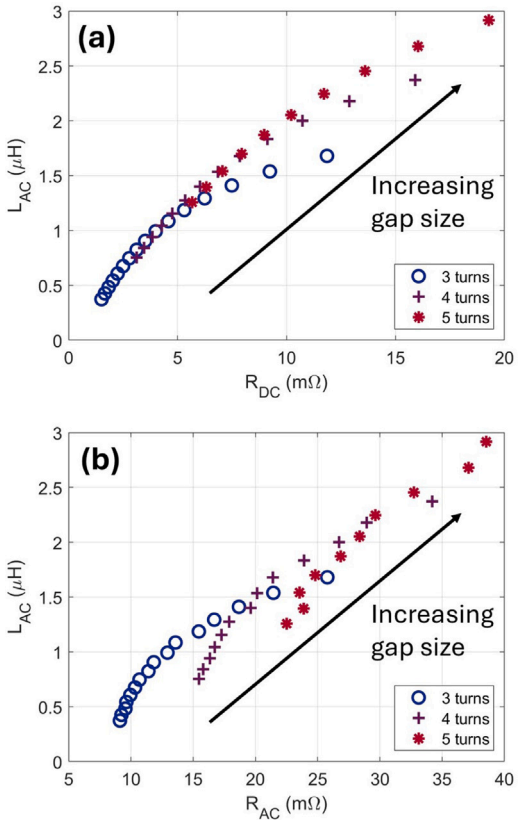

Fig. 4. L_{AC} at 500 kHz plotted as a function of (a) R_{DC} and (b) of R_{AC}. The data are obtained from inductor geometries with varying number of turns and varying gap size, all with d = 12.5 cm, s = 5 mm, and t = 0.5 mm. For 3 turns, g is varied in steps of 0.5 cm between 1 cm and 8.5 cm. For 4 turns, g is varied in steps of 0.5 cm between 1 cm and 7 cm. For 5 turns, g is varied in steps of 0.5 cm between 1 cm and 5.5 cm.

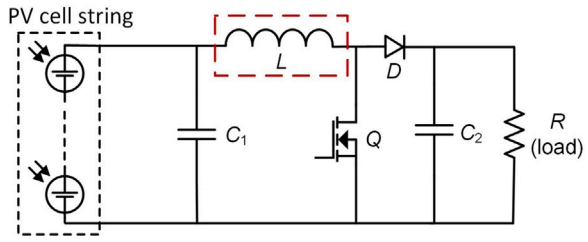

Fig. 5. String of series-connected solar cells at the input of a DC–DC boost converter. The inductor to be replaced by a planar inductor is highlighted. The capacitors, inductor, MOSFET, diode, and resistive load are represented by C, L, Q, D, and R, respectively.

properties for integration into a sub-module power converter. For this analysis, we assume that a string of series-connected solar cells is connected at the input of a DC–DC boost converter, which is a basic converter topology employed for MPPT in PV applications (Ayop and Tan, 2018). The schematic of this approach, with the inductor to be replaced by a planar inductor highlighted, is presented in Fig. 5.

In the DC–DC boost converter from Fig. 5, the input capacitor C_1 and the inductor L ensure that the PV cell string operates near its maximum power point. The inductor L reduces current ripple, while the capacitor C_1 minimizes voltage ripple. It is important to note that these components can partially compensate for each other; for instance, a lower capacitance may be offset by a higher inductance, and vice versa (Ayop and Tan, 2018). However, for the feasibility analysis in this section, certain assumptions are made. Specifically, it is assumed that the inductor must suppress the ripple current to a peak-to-peak value lower than 20% of the DC input current at the maximum power point (MPP) under Standard Test Conditions (STC), with a duty cycle of 0.5. Additionally, it is assumed that the input capacitor C_1 minimizes the voltage ripple to the desired level. This may be achieved by leveraging the solar-cell self-capacitance (van Nijen et al., 2022; Carigiet, 2022), or through the integration of a capacitor within the PV module (Van Dyck et al., 2024). It is shown in Appendix A that under these conditions, a switching frequency of approximately 4 MHz is required when only the self-inductance of a PV cell string is leveraged. In the present section, we investigate the feasibility of lowering this switching frequency to 250 kHz and 500 kHz by implementing planar air-core inductors. It is important to note that the number of solar cells in the string at the converter's input can vary, ranging from a single-cell string to a string with multiple cells. The length of the string has important implications for the required inductor properties. On the one hand, in short strings where the voltage is relatively low, the inductor only requires limited inductance to reduce the ripple current to the desired level. This is advantageous for the feasibility, as it was explained in Section 3.3 that a lower ohmic resistance can be achieved in inductors that require a lower inductance. On the other hand, for longer strings the inductor can be permitted to have a higher resistance. This is because the power losses in the inductor depend solely on the current and do not depend on the voltage. Consequently, to achieve low power losses in the inductor as a fraction of the generated power, a higher ohmic resistance is acceptable when the inductor is used with a longer solar-cell string. Considering these factors, the feasibility analysis is performed for different string lengths by following these steps:

1. A range of different inductor geometries is simulated in COMSOL at 1 Hz (representing DC conditions), 250 kHz, and 500 kHz. The inductor variations comprise different numbers of turns (3, 4, 5), gap sizes (1 cm - 8 cm), spacings (1 mm, 3 mm, 5 mm) and thicknesses (0.25 mm, 0.5 mm, 1 mm). For the different combinations of these parameters, we obtain the R_{DC}, L_{DC}, R_{AC}, and L_{AC}. The resulting L_{AC} values from these different inductor geometries range between 0.3 μH and 3.2 μH.
2. The solar-cell MPP parameters under STC are set at a V_{mpp} of 0.63 V and an I_{mpp} of 6 A. Using Eq. (A.1), we can evaluate for different solar-cell string lengths and frequencies what minimum inductance is required to suppress the ripple current below 20%. Using these results, we categorize the inductors based on their L_{AC} values for implementation into different string lengths at both 250 kHz and 500 kHz. Here, the self-inductance of the solar-cell string is not included in this analysis and we assume one inductor per string. Moreover, it is assumed that the inductor is implemented with the highest possible solar-cell string length, as long as it is able to suppress the ripple current below 20% at STC.
3. For each combination of an inductor and a given solar-cell string, we can calculate the ohmic losses in the inductor. The ohmic losses are based on the DC current, as well as on the AC ripple current. The method for calculating power losses in the inductor is described in Appendix B. Finally, we express the inductor ohmic losses as a fraction of power generated in the solar-cell string.

Fig. 6 presents the results of the feasibility analysis, showing the relative ohmic inductor losses as a fraction of the power generated in the solar-cell string for various string lengths. Fig. 6(a) shows the analysis at 250 kHz, whereas 6(b) illustrates the analysis at 500 kHz.

First of all, it follows from Fig. 6 that there is potential to integrate planar air-core inductors at the sub-module level to facilitate embedded power electronics. However, when comparing Fig. 6(a) and 6(b), it is evident that the lowest relative losses in the inductor are around 2% at 250 kHz, whereas they decrease to around 1% at 500 kHz. This occurs because as the frequency increases, a given inductor geometry compatible with a higher string length, thereby reducing the relative losses in

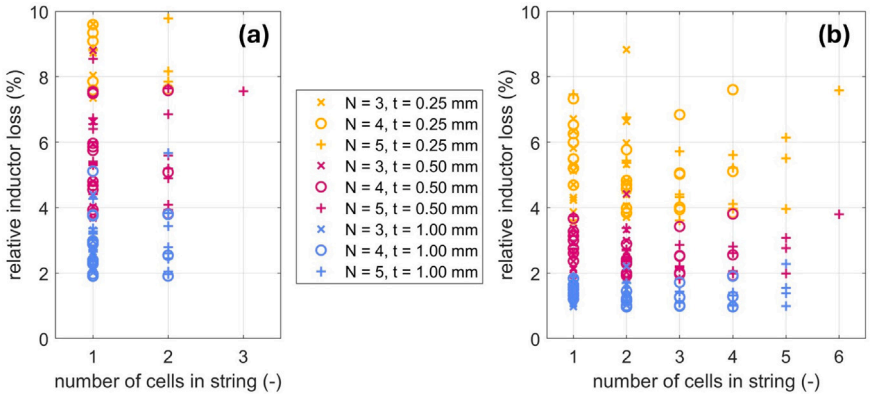

Fig. 6. Feasibility for inductor integration at (a) 250 kHz and (b) 500 kHz. All inductors have d = 12.5 cm, but comprise different numbers of turns (3, 4, 5), gap sizes (1 cm – 8 cm), spacings (1 mm, 3 mm, 5 mm) and thicknesses (0.25 mm, 0.50 mm, 1.0 mm). The losses are calculated under the assumption that the solar cell (string) is operating at the maximum power point in STC.

the inductor. This shows the importance of switching frequency as well as the number of series-connected cells for the feasibility assessment. It is worth noting that in both Fig. 6(a) and 6(b), the strings with the highest number of cells have only a few data points. This is because only a few of the simulated geometries have sufficient inductance to suppress the ripple to the desired level at these combinations of frequency and input voltage.

Moreover, the scattered data throughout the plots indicate that optimizing inductor parameters, such as the number of turns, spacing, and gap size, plays a crucial role in achieving the optimal design. Generally, it appears that inductors with a relatively low spacing of 1 mm achieve the lowest relative losses. This is because the DC losses are higher than the AC ohmic losses; typically, the AC losses only constitute a few percent of the total ohmic losses in the inductor. Additionally, the thickness t is a key factor in achieving the desired level of ohmic losses. For instance, at 500 kHz the lowest relative losses are approximately 4% at 0.25 mm thickness, 2% at 0.50 mm thickness, and 1% at 1.0 mm thickness. It is also worth noting that for both 250 kHz and 500 kHz, the lowest relative inductor loss remains fairly constant across different string lengths.

However, no conclusive statements can be made about whether these loss factors are 'good enough.' Adjustments to certain assumptions can significantly alter the data in Fig. 6. For instance, operating at higher frequencies or allowing a higher ripple current level would permit a lower minimum inductance. This would enable the use of an inductor with fewer turns and lower thickness, or the same inductor for a longer string length. Moreover, it is ultimately up to the power electronics designer to determine the desired converter efficiency, size, and cost. Nevertheless, this feasibility analysis provides a general indication of the potential role that planar air-core inductors can play in sub-module power converters. Overall, this study demonstrates that planar air-core inductors have the potential to be implemented into PV modules, enabling the removal of the inductor from the power converter. However, it is important to acknowledge that in most cases this requires that (1) the converter has a high switching frequency of multiple hundreds of kHz and (2) the inductor thickness is at least multiple hundreds of micrometer. Although the focus of this study is not on manufacturing, it must be noted that the required inductor thickness range surpasses the capabilities of screen printing, the primary technique employed by the PV industry for solar cell metallization (Tepner and Lorenz, 2023). Hence, alternative manufacturing methods should be explored for the planar inductor, such as cutting or etching copper foil (Ascari et al., 2023), or utilizing a form of additive manufacturing (Vafadar et al., 2021; Yan et al., 2016). These conditions present significant challenges for this solution to be widely adopted in the PV market. Nevertheless, this study can serve as a foundation for further research. For instance, it could be worthwhile to study the implementation of planar inductors in combination with leveraging the self-inductance of solar cells, thereby reducing the minimum inductance requirements from the inductor. Additionally, the high-frequency properties of the inductor could be enhanced by using alternative track structures, such as multitrack or Litz wire designs (Kolahian et al., 2024). Moreover, multiple inductors per string could be considered. Another approach could involve increasing inductance by utilizing planar inductors with ferromagnetic core material, potentially reducing the required number of turns and thickness. Furthermore, practical issues must be addressed if feasible combinations are identified. For example, thermal management and electromagnetic interference will need to be carefully considered in real-world applications.

5. Conclusion

In this study, it was investigated whether copper planar air-core inductors with an area of 12.5 cm × 12.5 cm can yield the required inductor properties to support sub-module power conversion in PV modules. First, it was shown how the interplay between the different design parameters, such as track spacing, track width, number of turns, and middle gap size, play an important role in the inductor properties. This analysis includes changes due to high-frequency effects, which significantly impact the results. Specifically, it was shown that a minimum track spacing of a few millimeters is necessary to limit the proximity effect at frequencies of 50 kHz and above. Additionally, it was observed that increasing the middle gap size or the number of turns can enhance the inductance, though both approaches come with the drawback of increased inductor resistance.

The coil geometries that were simulated yield inductance values between 0.3 μH and 3.2 μH. The feasibility of implementing these inductors into an exemplary DC–DC boost converter was evaluated. To adequately reduce the current ripple from a solar-cell string with such inductance values, a significant switching frequency of at least several hundred kHz is required. Moreover, at 500 kHz, an inductor thickness of around 0.5 mm is necessary to keep the ohmic losses in the inductor below 2% of the total generated power in standard test conditions. While demonstrating feasible combinations, these findings also present significant challenges for the sub-module integration of air-core planar inductors. For future research, several proposals were made to improve the inductor properties. These include incorporating ferromagnetic core materials or leveraging the self-inductance of the solar-cell string. Additionally, practical issues such as thermal management and electromagnetic interference will need to be carefully addressed in real-world applications.

CRediT authorship contribution statement

David A. van Nijen: Writing – review & editing, Writing – original draft, Visualization, Validation, Software, Project administration, Methodology, Investigation, Formal analysis, Data curation, Conceptualization. **Saurabh Chakravarty:** Validation, Software, Methodology, Investigation, Formal analysis, Data curation. **Jim Voorn:** Validation, Software, Methodology, Investigation, Formal analysis, Data curation. **Miro Zeman:** Funding acquisition. **Olindo Isabella:** Writing – review & editing, Supervision, Funding acquisition. **Patrizio Manganiello:** Writing – review & editing, Supervision, Project administration, Methodology, Formal analysis, Conceptualization.

Declaration of competing interest

The authors declare the following financial interests/personal relationships which may be considered as potential competing interests: P. Manganiello, D.A. van Nijen, and O. Isabella have a patent pending, which is assigned to TU Delft. If there are other authors, they declare that they have no known competing financial interests or personal relationships that could have appeared to influence the work reported in this paper.

Declaration of Generative AI and AI-assisted technologies in the writing process

During the preparation of this work the author(s) used ChatGPT in order to improve the text flow. After using this tool/service, the author(s) reviewed and edited the content as needed and take(s) full responsibility for the content of the published article.

Acknowledgments

This work is supported by the sector plan of the Dutch government in photovoltatronics research.

Appendix A. Exploiting solar cell self-inductance

For modern industrial c-Si solar cells, it is reported that the inductance of single-cell *laminates* is in the range of 63–130 nH, depending on the cell metallization pattern (van Nijen et al., 2023). Here it is important to note that the inductance of only the cell is lower than that of the full laminate, although its exact value is unknown. The minimal inductance of the inductor in a DC–DC boost converter can be calculated by Ayop and Tan (2018):

$$L_{min} = \frac{V_{mpp} D}{I_{mpp} \gamma_{I_L} f}, \tag{A.1}$$

where L_{min} is the minimum required inductance, V_{mpp} is the maximum power point voltage of the solar-cell string, D is the duty cycle of the converter, I_{mpp} is the maximum power point current of the string, and γ_{I_L} is the inductor current ripple factor. Hence, the product of I_{mpp} and γ_{I_L} is the peak-to-peak value of the ripple current. Moreover, f is the converter switching frequency. From Eq. (A.1) it can be deduced that in the boost converter, the inductance required to achieve a certain ripple current scales linearly with the number of series-connected cells. As such, it can be calculated irrespective of the string length from which frequency it becomes possible to replace the input inductor of a boost converter with the self-inductance of a solar-cell string. Here, it is assumed that the self-capacitance of the solar-cell string sufficiently reduces the voltage ripple (van Nijen et al., 2022). When considering typical values (V_{mpp} = 0.63 V, D = 0.5, I_{mp} = 6 A, γ_{I_L} = 0.2 and L = 65 nH), the minimum required frequency is approximately 4 MHz.

It is worth noting that there exist converters that specifically work at very high frequencies, such as soft-switched resonant converters, where the low switching losses allow for high switching frequency (Pilawa-Podgurski et al., 2009; Rashid et al., 2018). A study worth mentioning in this context is one in the low-power domain where the capacitive and inductive effects of a solar-cell string are used to replace the input capacitor and input inductor of a submodule integrated DC–DC converter (Huang et al., 2016). In their study, the operation is at a relatively high frequency of 5–10 MHz. Although this proves the concept of exploiting inductance in a solar-cell string, they conclude that it is clear that this type of approach may be less suitable for higher power applications because of the ripple currents and high switching frequencies required. Furthermore, it is worth noting that the control of resonant converters is more complicated than for hard-switched converters and the duty cycle cannot be varied as easily (Shen et al., 2016).

Appendix B. Inductor power loss calculation

To accurately calculate the power losses in an inductor, it must be considered that the inductor is subjected to a DC current with a superimposed AC current ripple. The conventional approach involves decoupling the losses associated with different frequency components. In this study, we only consider the fundamental frequency of the AC current and neglect the harmonics. Consequently, the total power loss can be expressed as follows:

$$P_{loss} = R_{DC} \times I_{DC}^2 + R_{AC} \times I_{AC,rms}^2 \tag{B.1}$$

where P_{loss} represents the power loss in the inductor, R_{DC} denotes the DC resistance, I_{DC} is the DC current, R_{AC} signifies the AC resistance, and $I_{AC,rms}$ is the root-mean-square (RMS) value of the AC current. In this study, we approximate the ripple current as a triangular waveform. Consequently, the $I_{AC,rms}$ can be derived from the peak-to-peak value of the ripple current, divided by a factor of $2\sqrt{3}$.

Data availability

The dataset underlying this article is available in the 4TU Research Database, accessible via this link: http://doi.org/10.4121/b7267f87-15b1-4c97-b9b2-e3aeb95393ac.

References

Acero, J., Carretero, C., Lope, I., Alonso, R., Lucia, O., Burdio, J.M., 2013. Analysis of the mutual inductance of planar-lumped inductive power transfer systems. IEEE Trans. Ind. Electron. 60 (1), 410–420.

Ascari, A., Angeloni, C., Liverani, E., Fortunato, A., 2023. High speed laser cutting of ultrathin metal foils for battery cell production. J. Laser Appl. 35 (4), 042063.

Ayop, R., Tan, C.W., 2018. Design of boost converter based on maximum power point resistance for photovoltaic applications. Sol. Energy 160, 322–335.

Benzidane, M.R., Melati, R., Benyamina, M., Meskine, S., Spiteri, P., Boukortt, A., Adda Benattia, T., 2022. Miniaturization and optimization of a DC-DC boost converter for photovoltaic application by designing an integrated dual-layer inductor model. Trans. Electr. Electron. Mater. 1–14.

Burger, B., Kranzer, D., 2009. Extreme high efficiency PV-power converters. In: 2009 13th European Conference on Power Electronics and Applications. pp. 1–13.

Calcabrini, A., Weegink, R., Manganiello, P., Zeman, M., Isabella, O., 2021. Simulation study of the electrical yield of various PV module topologies in partially shaded urban scenarios. Sol. Energy 225, 726–733.

Cao, Y., Groves, R., Huang, X., Zamdmer, N., Plouchart, J.-O., Wachnik, R., King, T.-J., Hu, C., 2003. Frequency-independent equivalent-circuit model for on-chip spiral inductors. IEEE J. Solid-State Circuits 38 (3), 419–426.

Carigiet, F., 2022. Inductive Power Transfer for Photovoltaic Modules (Ph.D. thesis). Friedrich-Alexander-Universität Faculty of Engineering.

Carigiet, F., Knecht, R., Baumann, T., Brabec, C.J., Baumgartner, F.P., 2018. New PV system concept: inductive power transfer for PV modules. In: 35th European Photovoltaic Solar Energy Conference and Exhibition.

Carigiet, F., Knecht, R., Baumann, T., Brabec, C.J., Baumgartner, F.P., 2019. New PV system concept : wireless PV module prototype. In: 36th European Photovoltaic Solar Energy Conference and Exhibition.

Casanova, J.J., Low, Z.N., Lin, J., Tseng, R., 2009. Transmitting coil achieving uniform magnetic field distribution for planar wireless power transfer system. In: 2009 IEEE Radio and Wireless Symposium. pp. 530–533. http://dx.doi.org/10.1109/RWS.2009.4957405.

Chang, A.H., Avestruz, A.-T., Leeb, S.B., 2015. Capacitor-less photovoltaic cell-level power balancing using diffusion charge redistribution. IEEE Trans. Power Electron. 30 (2), 537–546.

Coffin, J.G., 1906. The influence of frequency upon the self-inductance of coils. Proc. Am. Acad. Arts Sci. 41 (34), 789–803.

COMSOL, 2022. AC/DC module user's guide V6.1. https://doc.comsol.com/6.1/doc/com.comsol.help.acdc/ACDCModuleUsersGuide.pdf. (Last Accessed on 25 September 2024).

COMSOL Group, 2022. COMSOL multiphysics V6.1.

Deline, C., Sekulic, B., Stein, J., Barkaszi, S., Yang, J., Kahn, S., 2014. Evaluation of maxim module-integrated electronics at the DOE regional test centers. In: 2014 IEEE 40th Photovoltaic Specialist Conference. PVSC, pp. 0986–0991. http://dx.doi.org/10.1109/PVSC.2014.6925080.

Dhahri, Y., Ghedira, S., Besbes, K., 2016. Design of an integrated inductor with magnetic core for micro-converter DC-DC application. Trans. Electr. Electron. Mater. 17 (6), 369–374.

Dhahri, Y., Ghedira, S., Zrafi, R., Besbes, K., 2017. Design of an integrated inductor in micro-converter DC-DC for photovoltaic applications. In: 2017 International Conference on Engineering & MIS. ICEMIS, pp. 1–5. http://dx.doi.org/10.1109/ICEMIS.2017.8273058.

Golroodbari, S.Z.M., de Waal, A.C., van Sark, W.G.J.H.M., 2018. Improvement of shade resilience in photovoltaic modules using buck converters in a smart module architecture. Energies 11 (1).

Greenhouse, H., 1974. Design of planar rectangular microelectronic inductors. IEEE Trans. Parts Hybrids Packag. 10 (2), 101–109.

Huang, J.-H., Lehman, B., Qian, T., 2016. Submodule integrated boost DC-DC converters with no external input capacitor or input inductor for low power photovoltaic applications. In: 2016 IEEE Energy Conversion Congress and Exposition. ECCE, pp. 1–7. http://dx.doi.org/10.1109/ECCE.2016.7855476.

Imtiaz, A.M., Khan, F.H., 2012. AC solar cells: An embedded "all in one" PV power system. In: 2012 Twenty-Seventh Annual IEEE Applied Power Electronics Conference and Exposition. APEC, pp. 2053–2059. http://dx.doi.org/10.1109/APEC.2012.6166104.

Imtiaz, A.M., Khan, F.H., 2013. Light-generated effects on power switches used in a planar PV power system with monolithically embedded power converters. IEEE J. Photovolt. 3 (1), 394–400.

Imtiaz, A.M., Khan, F.H., Kamath, H., 2013. All-in-one photovoltaic power system: Features and challenges involved in cell-level power conversion in ac solar cells. IEEE Ind. Appl. Mag. 19 (4), 12–23.

Ki, W.-H., Ma, D., 2001. Single-inductor multiple-output switching converters. In: 2001 IEEE 32nd Annual Power Electronics Specialists Conference (IEEE Cat. No.01CH37230), vol. 1, pp. 226–231. http://dx.doi.org/10.1109/PESC.2001.954024.

Kolahian, P., Zarei Tazehkand, M., Baghdadi, M., 2024. Design and assessment of track structures in high-frequency planar inductors. Energies 17 (4).

Lai, J.-S., Nelson, D.J., 2007. Energy management power converters in hybrid electric and fuel cell vehicles. Proc. IEEE 95 (4), 766–777.

Lamers, M.W.P.E., Tjengdrawira, C., Koppes, M., Bennett, I.J., Bende, E.E., Visser, T.P., Kossen, E., Brockholz, B., Mewe, A.A., Romijn, I.G., Sauar, E., Carnel, L., Julsrud, S., Naas, T., de Jong, P.C., Weeber, A.W., 2012. 17.9% metal-wrap-through MC-Si cells resulting in module efficiency of 17.0%. Prog. Photovolt., Res. Appl. 20 (1), 62–73.

Leuenberger, D., Biela, J., 2017. PV-module-integrated AC inverters (AC modules) with subpanel MPP tracking. IEEE Trans. Power Electron. 32 (8), 6105–6118.

Li, J., Costinett, D., 2018. Analysis and design of a series self-resonant coil for wireless power transfer. In: 2018 IEEE Applied Power Electronics Conference and Exposition. APEC, pp. 1052–1059. http://dx.doi.org/10.1109/APEC.2018.8341145.

Low, Z.N., Casanova, J.J., Maier, P.H., Taylor, J.A., Chinga, R.A., Lin, J., 2010. Method of load/fault detection for loosely coupled planar wireless power transfer system with power delivery tracking. IEEE Trans. Ind. Electron. 57 (4), 1478–1486.

Low, Z.N., Chinga, R.A., Tseng, R., Lin, J., 2009. Design and test of a high-power high-efficiency loosely coupled planar wireless power transfer system. IEEE Trans. Ind. Electron. 56 (5), 1801–1812.

MacAlpine, S.M., Erickson, R.W., Brandemuehl, M.J., 2013. Characterization of power optimizer potential to increase energy capture in photovoltaic systems operating under nonuniform conditions. IEEE Trans. Power Electron. 28 (6), 2936–2945.

Mohan, S.S., del Mar Hershenson, M., Boyd, S.P., Lee, T.H., 1999. Simple accurate expressions for planar spiral inductances. IEEE J. Solid-State Circuits 34 (10), 1419–1424.

Nguyen, M.H., Fortin Blanchette, H., 2020. Optimizing AC resistance of solid PCB winding. Electronics 9 (5).

Olalla, C., Clement, D., Rodriguez, M., Maksimovic, D., 2013. Architectures and control of submodule integrated DC–DC converters for photovoltaic applications. IEEE Trans. Power Electron. 28 (6), 2980–2997.

Olalla, C., Deline, C., Maksimovic, D., 2014. Performance of mismatched PV systems with submodule integrated converters. IEEE J. Photovolt. 4 (1), 396–404.

Olalla, C., Maksimovic, D., Deline, C., Martinez-Salamero, L., 2017. Impact of distributed power electronics on the lifetime and reliability of PV systems. Prog. Photovolt., Res. Appl. 25 (10), 821–835.

Pilawa-Podgurski, R.C.N., Perreault, D.J., 2013. Submodule integrated distributed maximum power point tracking for solar photovoltaic applications. IEEE Trans. Power Electron. 28 (6), 2957–2967.

Pilawa-Podgurski, R.C.N., Sagneri, A.D., Rivas, J.M., Anderson, D.I., Perreault, D.J., 2009. Very-high-frequency resonant boost converters. IEEE Trans. Power Electron. 24 (6), 1654–1665.

Rashid, M.H., Hui, S.Y.R., Shu-Hung Chung, H., 2018. 12 - resonant and soft-switching converters. In: Rashid, M.H. (Ed.), Power Electronics Handbook (Fourth Edition), fourth ed. Butterworth-Heinemann, pp. 339–383. http://dx.doi.org/10.1016/B978-0-12-811407-0.00012-X.

Rieutort-Louis, W., Huang, L., Hu, Y., Sanz-Robinson, J., Wagner, S., Sturm, J.C., Verma, N., 2014. A complete fully thin-film PV harvesting and power-management system on plastic with on-sheet battery management and wireless power delivery to off-sheet loads. IEEE J. Photovolt. 4 (1), 432–439.

Rosa, E.B., 1908. The self and mutual inductances of linear conductors. Bull. Bureau Stand. 4, 301–344.

Shaltout, A.H., Gregori, S., 2020. Layout optimization of planar inductors for high-efficiency integrated power converters. Analog Integr. Circuits Signal Process. 102 (1), 155–167.

Shen, Y., Wang, H., Blaabjerg, F., Sun, X., Li, X., 2016. Analytical model for LLC resonant converter with variable duty-cycle control. In: 2016 IEEE Energy Conversion Congress and Exposition. ECCE, pp. 1–7. http://dx.doi.org/10.1109/ECCE.2016.7854882.

Stauth, J.T., Seeman, M.D., Kesarwani, K., 2012. A resonant switched-capacitor IC and embedded system for sub-module photovoltaic power management. IEEE J. Solid-State Circuits 47 (12), 3043–3054.

Sullivan, C.R., Sanders, S.R., 1996. Design of microfabricated transformers and inductors for high-frequency power conversion. IEEE Trans. Power Electron. 11 (2), 228–238.

Sunpower, 2022. Maxeon Gen III solar cells. https://cdn.enfsolar.com/Product/pdf/Cell/5b91fcf3916df.pdf?_ga=2.129740875.699501378.1555670092-1288217596.1555670091. (Last accessed on 26 March 2024).

Sze, S., 2002. Semiconductor Devices Physics and Technology, second ed. John Wiley & Sons, Inc.

Tepner, S., Lorenz, A., 2023. Printing technologies for silicon solar cell metallization: A comprehensive review. Prog. Photovolt., Res. Appl. 31 (6), 557–590.

Vafadar, A., Guzzomi, F., Rassau, A., Hayward, K., 2021. Advances in metal additive manufacturing: A review of common processes, industrial applications, and current challenges. Appl. Sci. 11 (3).

Van Dyck, R., Borgers, T., Govaerts, J., Poortmans, J., van Vuure, A.W., 2021. Three-dimensional multi-ribbon interconnection for back-contact solar cells. Prog. Photovolt., Res. Appl. 29 (5), 507–515.

Van Dyck, R., van Nijen, D., Muttillo, M., Manganiello, P., Bakovasilis, A., Borges, T., Onda, K., Zulhidza, R., Martinez, W., Sivaramakrishnan Radhakrishnan, H., Isabella, O., van Vuure, A.W., Poortmans, J., 2024. Photovoltaic module-integrated capacitors to facilitate embedded power electronics. In: 2024 IEEE 52nd Photovoltaic Specialist Conference. PVSC, pp. 0356–0358. http://dx.doi.org/10.1109/PVSC57443.2024.10749399.

van Nijen, D.A., Manganiello, P., Zeman, M., Isabella, O., 2022. Exploring the benefits, challenges, and feasibility of integrating power electronics into c-Si solar cells. Cell Reports Physical Science 3 (7), 100944.

van Nijen, D.A., Muttillo, M., Van Dyck, R., Poortmans, J., Zeman, M., Isabella, O., Manganiello, P., 2023. Revealing capacitive and inductive effects in modern industrial c-Si photovoltaic cells through impedance spectroscopy. Sol. Energy Mater. Sol. Cells 260, 112486.

van Nijen, D.A., Naoom, S., Muttillo, M., Procel, P., Zeman, M., Isabella, O., Manganiello, P., 2025. Analyzing the PN junction impedance of crystalline silicon solar cells across varied illumination and temperature conditions. Sol. Energy Mater. Sol. Cells 279, 113255.

van Nijen, D.A., Stevens, T., Mercimek, Y., Yang, G., van Swaaij, R.A., Zeman, M., Isabella, O., Manganiello, P., 2024. Combined fabrication and performance evaluation of TOPCon back-contact solar cells with lateral power metal-oxide-semiconductor field-effect transistors on a single substrate. Solar RRL 8 (9), 2300829.

Varghese, B.J., Smith, T., Azad, A., Pantic, Z., 2017. Design and optimization of decoupled concentric and coplanar coils for WPT systems. In: 2017 IEEE Wireless Power Transfer Conference. WPTC, pp. 1–4. http://dx.doi.org/10.1109/WPT.2017.7953838.

Wang, Y., Lucia, O., Zhang, Z., Gao, S., Guan, Y., Xu, D., 2020. A review of high frequency power converters and related technologies. IEEE Open J. Ind. Electron. Soc. 1, 247–260.

Wojda, R.P., Kazimierczuk, M.K., 2018. Winding resistance and power loss of inductors with Litz and solid-round wires. IEEE Trans. Ind. Appl. 54 (4), 3548–3557.

Yan, Y., Ding, C., Ngo, K.D.T., Mei, Y., Lu, G.-Q., 2016. Additive manufacturing of planar inductor for power electronics applications. In: 2016 International Symposium on 3D Power Electronics Integration and Manufacturing. 3D-PEIM, pp. 1–16. http://dx.doi.org/10.1109/3DPEIM.2016.7570536.

Ziar, H., Manganiello, P., Isabella, O., Zeman, M., 2021. Photovoltatronics: intelligent PV-based devices for energy and information applications. Energy Environ. Sci. 14, 106–126.